Tropospheric phase delay in interferometric synthetic aperture radar estimated from meteorological model and multispectral imagery

Béatrice Puysségur,[1] Rémi Michel,[1] and Jean-Philippe Avouac[2]

[1] ENVISAT Medium Resolution Imaging Spectrometer Instrument (MERIS) multispectral data and the mesoscale meteorological model MM5 are used to estimate the tropospheric phase delay in synthetic aperture radar (SAR) interferograms. MERIS images acquired simultaneously with ENVISAT Advanced Synthetic Aperture Radar data provide an estimate of the total water vapor content W limited to cloud-free areas based on spectral bands ratio (accuracy 0.17 g cm^{-2} and ground resolution 300 m). Maps of atmospheric delay, 2 km in ground resolution, are simulated from MM5. A priori pertinent cumulus parameterization and planetary boundary layer options of MM5 yield near-equal phase correction efficiency. Atmospheric delay derived from MM5 is merged with available MERIS W product. Estimates of W measured from MERIS and modeled from MM5 are shown to be consistent and unbiased and differ by $\sim$0.2 g cm^{-2} (RMS). We test the approach on data over the Lebanese ranges where active tectonics might contribute to a measurable SAR signal that is obscured by atmospheric effects. Local low-amplitude (1 rad) atmospheric oscillations with a 2.25 km wavelength on the interferograms are recovered from MERIS with an accuracy of 0.44 rad or 0.03 g cm^{-2}. MERIS water product overestimates W in the clouds shadow due to mismodeling of multiple scattering and underestimates W on pixels with undetected semitransparent clouds. The proposed atmospheric filter models dynamic atmospheric signal which cannot be recovered by previous filtering techniques which are based on a static atmospheric correction. Analysis of filter efficiency with spatial wavelength shows that $\sim$43% of the atmospheric signal is removed at all wavelengths.

1. Introduction

[2] From the phase difference of radar images acquired at different dates, Differential interferometric synthetic aperture radar interferometry (DInSAR) yields maps of ground displacement for various applications in tectonics, glaciology, volcanology, mining subsidence and landslide monitoring [*Hanssen*, 2001; *Massonnet et al.*, 1993]. Ground deformation is only one cause of phase changes in DInSAR and interferograms are affected by various noise sources originating from digital elevation model (DEM) errors, baseline and temporal decorrelation and by coherent noise like atmospheric effects [*Hanssen*, 2001] or noise related to orbits uncertainty. Coherent noise typically results in a few fringes per 100 km [*Massonnet and Rabaute*, 1993]. It does not affect too much the measurements of phenomenon inducing strong coherent gradients over relatively short wavelength (a few kilometers to a few tens of kilometers)

such as coseismic deformation [*Massonnet et al.*, 1993] or rapid glacier flow [*Rignot et al.*, 2004]. However, the pattern and amplitude of atmospheric phase delays put tight limitation on the measurement of the low amplitude and large spatial wavelengths signal related to interseismic deformation [*Wright et al.*, 2004]. This source of noise is particularly limiting because interseismic deformation and atmospheric delay tend to be correlated with topography [*Remy et al.*, 2003]. Topography indeed influence atmospheric conditions and is merely the result of tectonic deformation cumulated over a geologic period of time.

[3] Several studies already analyzed the ionospheric and tropospheric signal on differential SAR interferometry [e.g., *Emardson et al.*, 2003; *Hanssen et al.*, 1999; *Lohman and Simons*, 2005; *Williams et al.*, 1998]. Several atmospheric phase screen filters have been proposed: *Delacourt et al.* [1998] proposed an elevation-dependent filter based on a simplified static model of the atmosphere constrained by ground meteorological data. In this approach, for a given study area and date, the radar delay is only elevation-dependent; *Remy et al.* [2003] proposed models of the tropospheric phase delay that vary linearly or nonlinearly with elevation; another approach consists in reducing the contribution of the atmospheric phase delay by stacking

---

[1] Laboratoire de Détection et de Géophysique, CEA, Bruyères-le-Châtel, France.
[2] Tectonics Observatory, Geological and Planetary Sciences Division, California Institute of Technology, Pasadena, California, USA.

numerous interferograms (generally tens of interferograms are required, making this approach quite expensive in terms of data acquisition and computation) [*Wright et al.*, 2001]. Rather complex atmospheric signals resulting from the dynamics of the atmosphere are in fact common in InSAR [*Hanssen et al.*, 2000] and severely limit the effectiveness of these approaches. For example, *Hanssen et al.* [2000] report clear InSAR signals due to convective rolls at the kilometric scale, even under clear-sky conditions. The above mentioned filters do not take into account the regional variability of the atmosphere and are therefore incapable of removing such effects. In addition, regional effects can be stationary so that they are not efficiently reduced by stacking (noise reduction is obtained only if the errors in the various interferograms are not correlated). The development of a comprehensive filter of the atmospheric contribution in InSAR thus remains a challenge. Some authors have developed atmospheric radar delay estimation methods using meteorological modeling [*Bonforte et al.*, 2001], multispectral imagery [*Li et al.*, 2006a, 2006b, 2005; *Moisseev and Hanssen*, 2003] or GPS [*Li et al.*, 2006c].

[4] In the present study we analyze the potential of the Mesoscale Meteorological Model, MM5, [*Grell et al.*, 1995] and of multispectral Medium Resolution Imaging Spectrometer Instrument (MERIS) images (the MERIS system is on board the ENVISAT platform [*European Space Agency (ESA)*, 2004]) to compensate for the tropospheric contribution on SAR interferograms. We use 11 ENVISAT Advanced Synthetic Aperture Radar (ASAR) and ENVISAT MERIS images acquired simultaneously over Lebanon. The interferograms present large atmospheric effects resulting from contrasted topography nearby the Mediterranean Sea (Figure 1 and Table 1). This area is of interest for tectonic studies and seismic hazard given the activity of the Levantine Fault and of the various thrust faults bounding the Lebanon ranges, with interseismic velocities estimated to only a few millimeters per year [*Daëron et al.*, 2004; *Klinger et al.*, 2000].

[5] In section 2 we present the equation of the tropospheric phase delay and characteristics of MERIS multispectral imagery and of the meteorological mesoscale model MM5 that are of interest for our study. In section 3 we develop an approach to estimate the radar phase delay using the meteorological mesoscale model MM5 and additionally available clear sky multispectral MERIS images. A comparison of the water vapor content independently estimated by MM5 and MERIS is carried out in section 4 in order to investigate biases and uncertainties. In section 5, our approach, which takes into account the dynamics of the atmosphere, is compared to the filtering based on a static atmospheric model [*Delacourt et al.*, 1998] and to stacking. The results of our atmospheric correction for interferograms over Lebanon are presented and discussed in section 6.

2. Background

2.1. Equation of the Phase Delay

[6] The radar phase delay depends on the refractivity index N of the atmosphere, that can be written as

$$N = (n-1) \times 10^6 = k_1 \frac{P}{T} + k_2 \frac{e}{T} + k_3 \frac{e}{T^2} + k_4 W_{\text{cloud}} + k_5 \frac{n_e}{f^2},$$

(1)

where n is the refraction index of air at radio frequencies, P is the total pressure (mbar), e is the water vapor partial pressure (mbar), T is the temperature (K), W_{cloud} is the cloud water content (g m^{-3}), n_e is the electronic density of the ionosphere, and f is the radar frequency [*Smith and Weintraub*, 1953]; $k_1 = 77.6$ K mbar^{-1}, $k_2 = -6.0$ K mbar^{-1}, $k_3 = 3.75 \times 10^5$ K^2 mbar^{-1} are taken from *Smith and Weintraub* [1953], k_4 was approximated to 1.45 m^3 g^{-1} by *Solheim et al.* [1999] from Clausius-Mossotti equation and $k_5 = -4.03 \times 10^7$ s^{-2} m^3 [*Skone and Cannon*, 1999]. The term $k_1 (P/T)$ is called the dry delay and the wet delay is the sum of three terms:

$$\left(k_2 \frac{e}{T} + k_3 \frac{e}{T^2} + k_4 W_{\text{cloud}} \right).$$

[7] The two-way radar phase delay φ in meters writes

$$\varphi = \frac{2 \times 10^{-6}}{\cos \theta} \int_h^H N(z)dz,$$

(2)

where θ is the satellite viewing zenith angle, h is the surface elevation, and H is the top elevation of the atmosphere.

[8] The ionospheric contribution to the index refractivity, $k_5(n_e/f^2)$, can be derived from GPS [*Ducic*, 2004]. Addressing this issue is beyond the scope of the present study.

[9] The water vapor content W (g cm^{-2}) can be derived from multispectral images (e.g., MERIS) and can be expressed as

$$W = 10 \frac{M_w}{R} \int_h^H \frac{e}{T} dz,$$

(3)

where M_w is the molar mass of water (18.0152×10^{-3} kg mol^{-1}), R the perfect gas constant (8.314 J.K^{-1} mol^{-1}), e the water vapor partial pressure (mbar), T the temperature (K).

[10] *Askne and Nordius* [1987] defined a mean temperature T_m of the atmosphere as

$$T_m = \frac{\int_h^H \frac{e}{T} dz}{\int_h^H \frac{e}{T^2} dz}.$$

(4)

[11] The phase delay can then be expressed as

$$\varphi = \frac{2 \times 10^{-6}}{\cos \theta} \left(\int_h^H k_1 \frac{P}{T} + \frac{RW}{10M_w} \left(k_2 + \frac{k_3}{T_m} \right) + \int_h^H k_4 W_{\text{cloud}} \right).$$

(5)

[12] The estimation of phase delay from MERIS and MM5 combined approach is based on this equation (see section 3.2).

2.2. MERIS

[13] MERIS is the Medium Resolution Spectrometer onboard ENVISAT platform [*ESA*, 2004], together with ASAR (Advanced Synthetic Aperture Radar) instrument. This passive multispectrometer has 15 bands from 395 nm
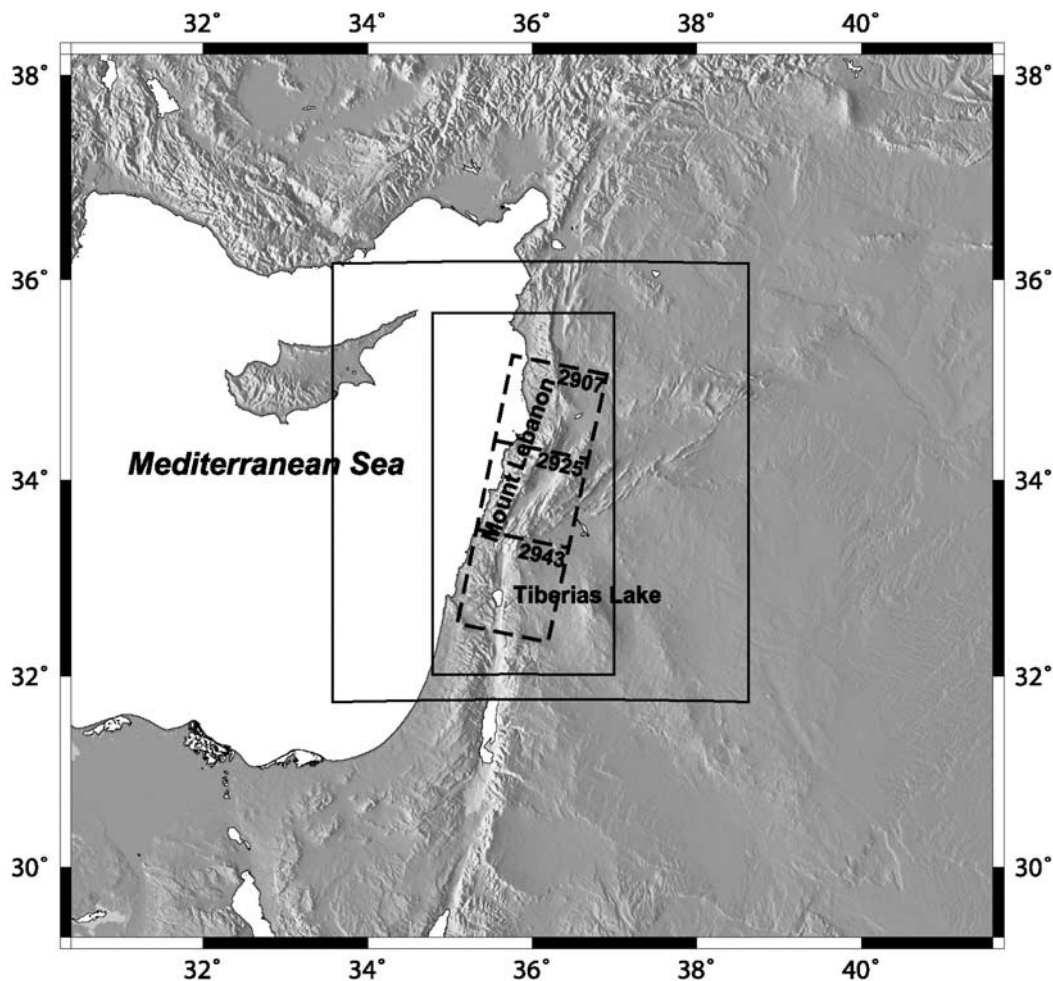
Figure 1. Three nested MM5 simulation domains. The full area was modeled with an 18 km resolution, and the two solid line boxes correspond to domains with 6 and 2 km resolution, respectively. Forty-two vertical levels were used in each simulation. Input is from NCEP reanalysis. Strong meteorological variability is induced by highly contrasted topography nearby the Mediterranean Sea (Mount Lebanon culminates at 3090 m and Tiberias Lake lies 209 m under sea level). Dashed line boxes delimit location of radar images frames 2907, 2925, and 2943.

to 900 nm. The MERIS full-resolution products have a 300 m ground resolution. In most cases, MERIS and ASAR data can be acquired simultaneously. The integrated amount of atmospheric water can be estimated from the ratio of the radiances measured at the edge (band 14 at 885 nm) and at the center (band 15 at 900 nm), respectively, of a water absorption band [*Fischer and Bennartz*, 1997]. *Fischer and Bennartz* [1997] developed an algorithm to estimate the water vapor content which is based on this principle and dedicated to MERIS. They distinguish three different cases: above cloud-free land surfaces, above the top of clouds, and above water. Hereafter, we describe the equation from *Fischer and Bennartz* [1997] for land pixels in cloud-free context.

[14] Let us note W_{MERIS} the water vapor content (g cm^{-2}) estimated from MERIS data by *Fischer and Bennartz* [1997] algorithm. It writes

$$W_{\mathrm{MERIS}} = k_0 + k_1 \log\left(R_{Ch15/Ch14}\right) + k_2 \log^2\left(R_{Ch15/Ch14}\right), \quad (6)$$

where $R_{Ch15/Ch14}$ denotes the radiance ratio between channels 15 and 14, the k_i are regression constants

depending on the solar zenith angle, the satellite zenith angle, the azimuth angle difference between sun and satellite and the surface pressure. This equation is based on a simple scattering model adjusted to real data by the way of the second-order term and the regression constants.

[15] The algorithm theoretical one-sigma accuracy is 0.17 g cm^{-2} [*Bennartz and Fischer*, 2001], which corresponds to a wet phase delay of 2.46 rad for a standard mean temperature T_m = 290 K and for ENVISAT ASAR frequency (5.331 GHz). The estimate of W is limited to pixels with a cloud-free atmosphere, which can be selected using the cloud mask provided with MERIS images.

2.3. MM5

[16] MM5 is a nonhydrostatic mesoscale meteorological model produced by National Center for Atmospheric Research (NCAR)/Pennsylvania State University, designed to simulate atmospheric circulation [*Grell et al.*, 1995]. The vertical coordinates are terrain-following sigma coordinates. They are function of top of atmosphere pressure and surface pressure at each point. They closely follow the surface for

Table 1. ENVISAT ASAR and MERIS Data Used[a]

Date	Orbit
4 Jan 2004	09651
19 Jan 2003	04641
27 Feb 2005	15663
14 Mar 2004	10653
30 Mar 2003	05643
27 Jun 2004	12156
13 Jul 2003	07146
1 Aug 2004	12657
5 Sep 2004	13158
10 Oct 2004	13659
26 Oct 2003	08649

[a]Frames 2907, 2925, and 2943 and track 78.

lower levels and get flatter and less resolved toward the top of atmosphere. MM5 has a multiple-nest capability and a variety of modeling options. MM5 meteorological input data consist of reanalyzed data, spatially and temporally interpolated to fit our region and dates of interest. Reanalysis data are a set of meteorological parameters on a regular geographic and time sampling. They are obtained by assimilation of several meteorological measurements from ground stations, aircraft, rawinsondes, satellites, ships and other sources [*Kistler et al.*, 1999]. The meteorological measurements include pressure, temperature, humidity, wind speed and direction.

[17] Other input data for MM5 are land use maps, elevation model, land-water mask, soil types, vegetation fraction and deep soil temperature. MM5 can run on several nested domains (see Figure 1) with increasing resolution to account for large-scale effects in the first low-resolution domain and for local effects in the fine-resolution domains. Reanalysis data is assimilated every six hours. We did not use MM5 assimilation option of ground meteorological data because it can introduce some artefacts in the simulations due to the local significance of meteorological surface measurements [*Stauffer et al.*, 1991].

[18] Output include temperature T (K), total pressure P (mbar), water vapor mixing ratio Q (kg kg^{-1}) and cloud water mixing ratio Q_{cloud} (kg kg^{-1}). The water vapor partial pressure e (mbar) and the cloud water content W_{cloud} (g m^{-3}) are computed from [*American Meteorological Society* (*AMS*), 2000]

$$e = \frac{QP}{0.622 + Q} \qquad (7)$$

and

$$W_{cloud} = \frac{Q_{cloud}(P - e)M_{dry}100}{RT}, \qquad (8)$$

where $M_{dry} = 28.966$ g mol^{-1} is the molar mass of dry air.

[19] We simulated the state of the atmosphere for each radar acquisition on our region of interest in order to estimate the tropospheric phase delay (see Table 1). The input reanalysis data we used is National Centers for Environmental Prediction (NCEP) Global Tropospheric Analyses "FNL" with resolution 1° × 1° since September 1999 [*Kistler et al.*, 1999]. Spatiotemporal parameters of the model were derived from experience [*Grell et al.*, 1995; C.

Millet, personal communication, 2004]. We have run MM5 (version 3.7) on 3 nested domains with resolution 18 km, 6 km and 2 km (see Figure 1) and with 42 vertical sigma levels σ (σ = 0.000000, 0.100000, 0.200000, 0.300000, 0.400000, 0.500000, 0.550000, 0.600000, 0.650000, 0.700000, 0.750000, 0.800000, 0.808018, 0.820248, 0.831866, 0.842902, 0.853386, 0.863345, 0.872805, 0.881792, 0.890329, 0.898439, 0.906143, 0.913462, 0.920414, 0.927018, 0.933292, 0.939251, 0.944912, 0.950290, 0.955399, 0.960252, 0.964862, 0.969242, 0.973402, 0.977354, 0.981108, 0.984674, 0.988062, 0.991280, 0.994337, 0.997241). Simulations are run from the day preceding the radar acquisition at 0600 UTC for 26 hours as the radar images are acquired at 0745 UTC. Note that negative altitudes near Tiberias Lake, which lies 209 m under sea level, were not correctly taken into account in the MM5 "TERRAIN" program because they were set to zero. The TERRAIN files were therefore corrected using codes from *Rögnvaldsson* [2005] in order to solve the problem.

[20] MM5 permits a variety of physical parameterizations concerning formation of cumulus, planetary boundary layer (PBL), moisture scheme, radiation scheme and surface scheme. We have tested several parameterizations for the formation of cumulus (Grell [*Grell et al.*, 1995], Fritsch-Chappell [*Fritsch and Chappell*, 1980], Kain-Fritsch [*Kain and Fritsch*, 1993]), for the planetary boundary layer model (Eta [*Janjic*, 1990, 1994], Hong-Pan [*Hong and Pan*, 1996], Pleim-Chang [*Pleim and Chang*, 1992]) and for the soil parameterization (five-layer model [*Dudhia*, 1996], Pleim-Xiu [*Xiu and Pleim*, 2001]) (see section 3.1). Pleim-Chang PBL model is coupled with Pleim-Xiu soil parameterization. We have run MM5 with widely used simple ice moisture scheme (Dudhia [*Grell et al.*, 1995]). The orographic shadowing effect has been taken into account, as well as the cloud-radiation scheme and the shallow cumulus option that handles nonprecipitating clouds.

3.   Estimation of Phase Delay

[21] The phase delay can be modeled from MM5 simulation results as described in section 3.1. In clear-sky conditions, for the case of ENVISAT ASAR images, this model can also account for the total water vapor content W derived from MERIS measurements, as explained in section 3.2.

3.1.   Estimation of Phase Delay From MM5

[22] Temperature T, water vapor mixing ratio Q, cloud water mixing ratio Q_{cloud} and pressure P are modeled by MM5. MM5 output grids are given on Lambert conformal grid and on sigma level coordinates. Because of sigma level dependence on DEM, the vertical sampling varies for each simulation point. For computational simplicity, MM5 output grids are projected on plane vertical levels with 10 m spacing for heights under a threshold altitude a_{max} and with

Table 2. MM5 Parameterizations for Planetary Boundary Layer (Same for the Three Domains) and Surface Scheme

Configuration	PBL Scheme	Surface Scheme
1	Hong-Pan	five-layer
2	Pleim-Chang	Pleim-Xiu
3	Eta	five-layer

Table 3. Comparison of Mean and Standard Deviation Between Water Vapor Content W Estimated by MERIS (W_{MERIS}) or MM5 (W_{MM5})[a]

	4 Jan 2004		19 Jan 2003		27 Feb 2005		14 Mar 2004		30 Mar 2003		27 Jun 2004		13 Jul 2003		1 Aug 2004		5 Sep 2004		10 Oct 2004		26 Oct 2003		Mean on All Tested Dates	
	$\overline{W}$	$\sigma(W)$	$\overline{W}$	$\sigma(W)$	$\overline{W}$	$\sigma(W)$	$\overline{W}$	$\sigma(W)$	$\overline{W}$	$\sigma(W)$	$\overline{W}$	$\sigma(W)$	$\overline{W}$	$\sigma(W)$	$\overline{W}$	$\sigma(W)$	$\overline{W}$	$\sigma(W)$	$\overline{W}$	$\sigma(W)$	$\overline{W}$	$\sigma(W)$	$\overline{W}$	$\sigma(W)$
$\overline{W}_{MM5}$, $\sigma(W_{MM5})$, g cm^{-2}																								
PBL 1	0.79	0.18	0.83	0.18	1.29	0.23	0.88	0.26	0.96	0.21	1.70	0.52	1.24	0.56	1.28	0.46	1.74	0.77	1.35	0.48	1.98	0.29	1.28	0.38
PBL 2	-	-	-	-	-	-	0.80	0.20	-	-	1.66	0.49	-	-	1.25	0.43	-	-	-	-	-	-	1.23	0.37
PBL 3	0.81	0.18	0.84	0.18	-	-	-	-	1.00	0.23	1.67	0.52	-	-	-	-	-	-	-	-	1.97	0.28	1.26	0.28
$\overline{W}_{MERIS}$, $\sigma(W_{MERIS})$, g cm^{-2}	0.74	0.19	0.62	0.15	1.23	0.30	0.89	0.25	0.89	0.30	1.75	0.57	1.12	0.58	1.25	0.60	1.92	0.87	1.77	0.48	1.53	0.33	1.25	0.42
$\overline{W}_{MM5}-\overline{W}_{MERIS}$, $\sigma(W_{MM5}-W_{MERIS})$, g cm^{-2}																								
PBL 1	0.055	0.20	0.21	0.14	0.064	0.18	-0.0066	0.16	0.069	0.15	-0.054	0.19	0.12	0.25	0.025	0.31	-0.18	0.27	-0.42	0.27	0.45	0.28	0.036	0.21
PBL 2	-	-	-	-	-	-	-0.095	0.14	-	-	-0.090	0.21	-	-	-0.0060	0.31	-	-	-	-	-	-	-0.063	0.22
PBL 3	0.0719	0.18	0.23	0.14	-	-	-	-	0.11	0.16	-0.085	0.21	-	-	-	-	-	-	-	-	0.44	0.30	0.15	0.20

	4 Jan 2004	19 Jan 2003	27 Feb 2005	14 Mar 2004	30 Mar 2003	27 Jun 2004	13 Jul 2003	1 Aug 2004	5 Sep 2004	10 Oct 2004	26 Oct 2003	Mean on All Tested Dates
Score 1												
PBL 1	0.42	0.67	0.81	0.80	0.88	0.94	0.91	0.87	0.95	0.84	0.60	0.79
PBL 2	-	-	-	0.83	-	0.93	-	0.87	-	-	-	0.91
PBL 3	0.49	0.69	-	-	0.85	0.93	-	-	-	-	0.53	0.70
Score 2												
PBL 1	0.83	0.81	0.84	0.81	0.90	0.94	0.91	0.87	0.95	0.85	0.79	0.86
PBL 2	-	-	-	0.85	-	0.93	-	0.87	-	-	-	0.92
PBL 3	0.83	0.83	-	-	0.87	0.93	-	-	-	-	0.74	0.84
Surface of undetected clouds,%	17.6	17.3	6.9	0.7	4.6	0	0	0	0	0.8	18.0	6.0

[a]W is in units of g cm^{-2}. Each line referring to MM5 divided into three lines comparing planetary boundary layer (PBL)/surface schemes (see Table 2). Dash denotes not tested configurations. Standard deviation of $W_{MM5}-W_{MERIS}$ is consistent with uncertainty on W_{MERIS} (0.17 g cm^{-2} [Bennartz and Fischer, 2001]) except on days with undetected clouds and for 10 October 2004. Correlation scores between W_{MERIS} and W_{MM5} including automatically undetected clouds (score 1) and with clouds manually discarded (score 2). The score dramatically improves when automatically undetected cirrus covering parts of the image (4 January 2004, 19 January 2003, 26 October 2003) are removed.
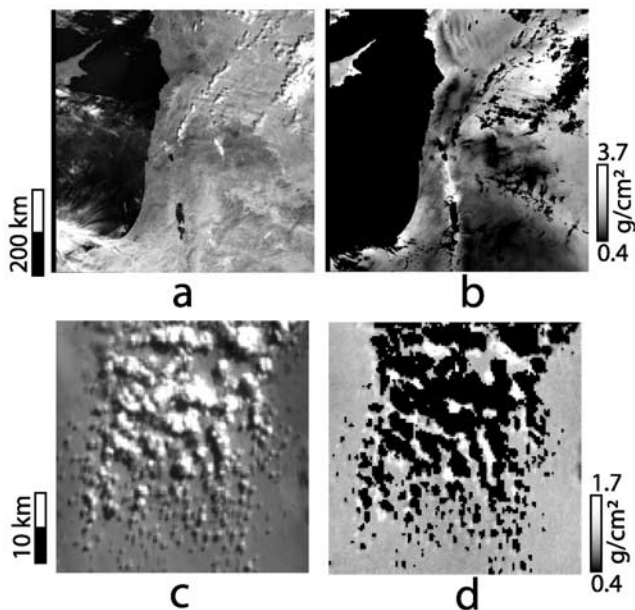
Figure 2. (a) MERIS channel 15 on 26 October 2003. (b) W_{MERIS} on the same date computed from *Fischer and Bennartz* [1997]. Cloudy and water pixels are masked in black. W highly depends of surface elevation. Note the gravity waves at the top center of the image. (c) MERIS channel 15 on 14 March 2004 (zoom). (d) W_{MERIS} for 14 March 2004 on the same frame as Figure 2c. W estimated on the shadow of clouds is greater than on neighboring pixels due to the simple refraction model (see section 3.2 for details).

increasing spacing beyond. a_{max} is set to $a_{max} = h_{max} + 500$ (m), where h_{max} is the maximum altitude on MM5 simulation area. The meteorological parameters are finally projected onto geographical grids.

[23] The phase delay is computed from these meteorological parameters using equations (1), (2), (7), and (8). The delay is integrated along the radar path from the satellite to the surface point using orbits and Shuttle Radar Topography Mission (SRTM) DEM projected onto radar geometry. SRTM DEM data voids have been filled in using neighboring pixels.

[24] Various cumulus parameterizations have been tested on the first simulation domain because the two smaller domains with resolution smaller than 10 km cannot support a cumulus parameterization. Amongst the proposed parameterizations, Grell, Fritsch-Chappell, Kain-Fritsch and Kain-Fritsch 2 schemes were compliant with the domain resolution (18 km). We tested the first three and found that Fritsch-Chappell scheme was unstable. Grell and Kain-Fritsch schemes yielded differences in the phase delay with a standard deviation of 0.99 rad (i.e., about 0.07 g cm^{-2}) and in our case no parameterization appears to be the most efficient. Thus we decided to run MM5 with Kain-Fritsch cumulus parameterization.

[25] Several planetary boundary layer models have been tested as well (Hong-Pan, Pleim-Chang and Eta models, see Table 2) but we did not found any preferable model as the relative quality of the results is date-dependent (see Table 3). We thus decided to run MM5 with Hong-Pan PBL model and five-layer soil moisture scheme.

3.2. Estimation of Phase Delay From MERIS and MM5

[26] The water vapor content W retrieved from MERIS allows to compute only the first term of the wet phase delay [*Askne and Nordius*, 1987; *Emardson and Derks*, 2000] (see equation (5)). The dry term cannot be retrieved from MERIS and as in section 3.1, we use MM5 simulations to compute this term. The second term of the wet delay depends on W and on the mean temperature T_m which is not provided by MERIS either. We thus compute T_m using MM5 simulations from equation (4). W_{MERIS} and T_m are projected on a geographic grid and the wet delay is derived using equation (5) and projected onto the radar geometry. The delay due to clouds is not estimated because W_{MERIS} is not available on cloudy pixels.
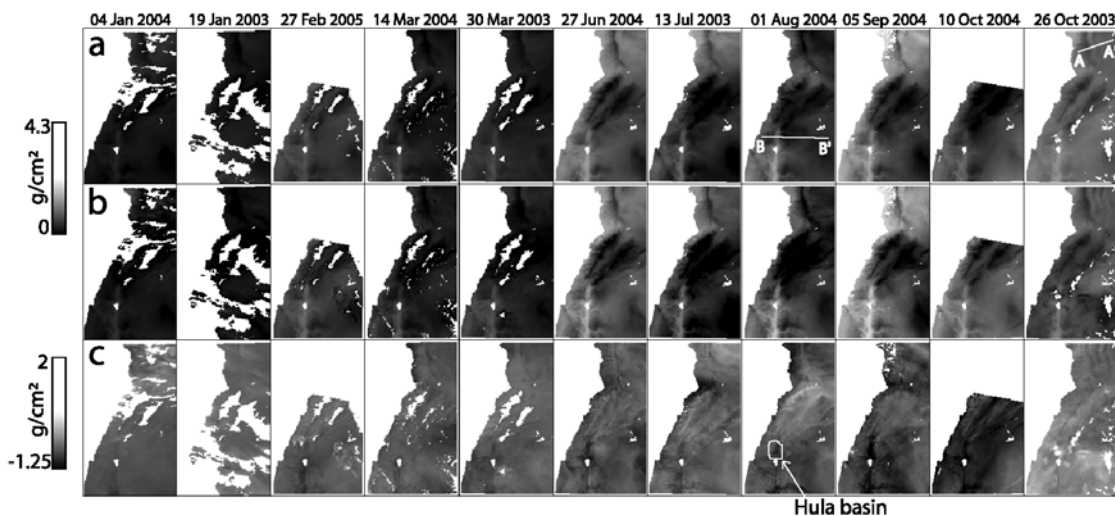

Figure 3. (a) W (g cm^{-2}) simulated by MM5 for 11 dates with configuration 1 (see Table 2). (b) W simulated by MERIS (same gray scale). (c) Difference between Figures 3a and 3b (different gray scale). Masked areas correspond to water or cloud pixels detected by MERIS. Simulations are generally very similar, except on cloudy pixels not detected by MERIS. Profiles AA′ (26 October 2003) and BB′ (1 August 2004) are shown on Figure 4.
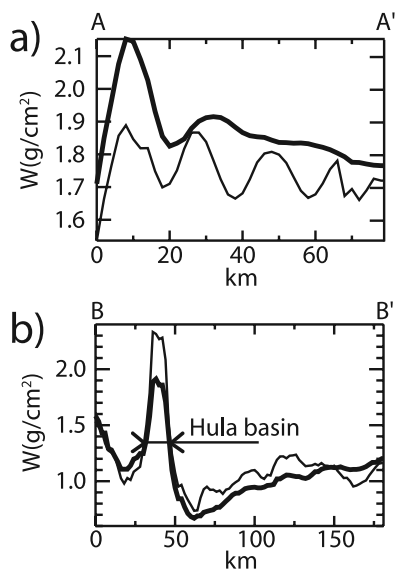
Figure 4. (a) AA′ profile of W (g cm^{-2}) on 26 October 2003 showing gravity waves. MERIS (thin line) clearly shows these waves, and MM5 (thick line) only reproduces two out of the four oscillations. Bias equals 0.127 g cm^{-2}, and the standard deviation of the difference is 0.076 g cm^{-2}. (b) BB′ profile on 1 August 2004. Simulations agree well except above Hula basin which was most probably irrigated. MM5 estimates less water than MERIS due to not modeled fine-scale (below 20 km) anthropogenic factors including irrigation. See Figure 3 for location of profiles.

[27] Estimation of W from MERIS can suffer from a bias in some parts of the image. Indeed, W_{MERIS} appears overestimated under the clouds shadow by an average factor 1.16 (see Figures 2c and 2d). This factor is the average W_{MERIS} on shadowed areas over the average W_{MERIS} on nonshadowed areas neighboring shadowed areas. This phenomenon results from the inadequacy of the single scatter-

ing model for radiative transfer equation within those areas where no direct incident light reaches the ground. Value of the image for those areas results from multiple scattered light only. Because the optical path of multi scattered light is longer than that of direct light, multi scattered light encounters more absorbent water vapor molecules and the resulting estimate of W suffers a positive bias. We estimated W from simulated shadowed and nonshadowed pixels with an ad hoc radiative transfer procedure [*Marion et al.*, 2006] and found a ratio of W equal to 1.22 that is consistent with the overestimate equal to 1.16 noted on Figure 2. An underestimate of W occurs for cloudy pixels not detected by MERIS algorithm. These clouds are generally semitransparent cirrus or cloud edges and the pixels radiance is the sum of the contribution from light coming from the surface and from the top of cloud. Thus the estimated columnar water vapor is between the water vapor content from the top of cloud and the water vapor content above surface and is underestimated. This highlights the fact that enhanced radiative transfer method should be used to improve the estimate of W.

4. Comparison of W Estimated From MERIS and Modeled by MM5

[28] In order to estimate the quality of water vapor content W estimated from MERIS and MM5 model with several physical parameterizations (see Table 2), we propose to compare them in this section. Results are presented in Figure 3 and Table 3. Estimates from MM5 and MERIS differ by 0.21 g cm^{-2} (RMS). This is consistent with the reported uncertainty on MERIS product (0.17 g cm^{-2}) [*Bennartz and Fischer*, 2001].

[29] In some cases, MM5 shows the ability to simulate fine-scale dynamical meteorological patterns: Two out of the four gravity or instability waves on 26 October 2003 superimpose on those calculated by MERIS (Figures 3 and 4). They are about 20 km in wavelength and are induced by the topography of the Syrian Coastal Ranges.
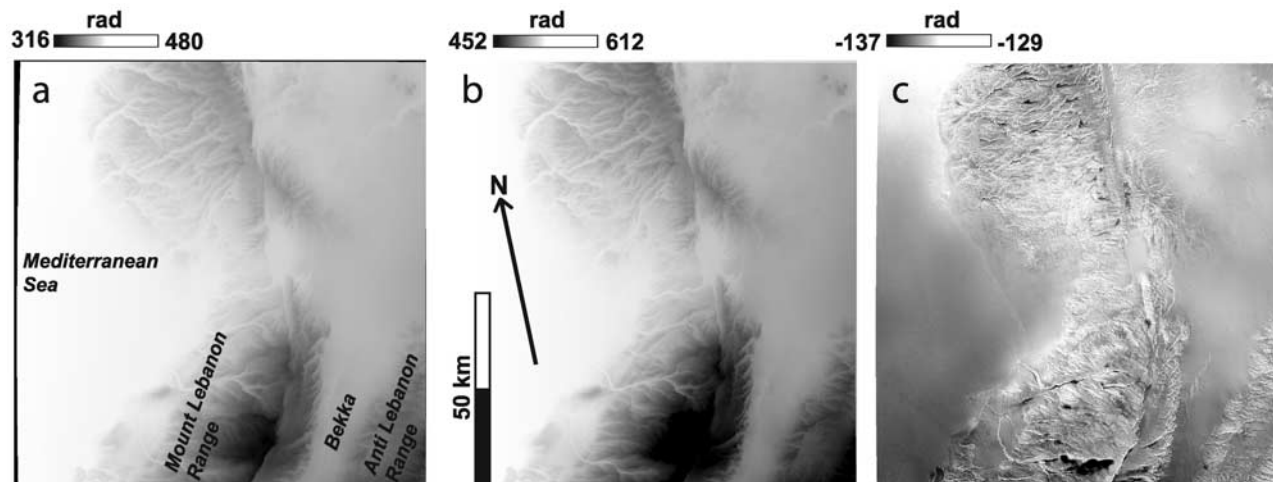

Figure 5. (a) Mean atmospheric radar delay modeled by MM5 averaged on 10 dates over frame 2907. (b) Same as Figure 5a with atmospheric delay modeled from *Delacourt et al.* [1998]. (c) Difference between delays in Figures 5a and 5b. Stationary meteorological patterns are evidenced, in particular, more humidity between Mount Lebanon and the sea and a drier atmosphere in the Bekka valley.
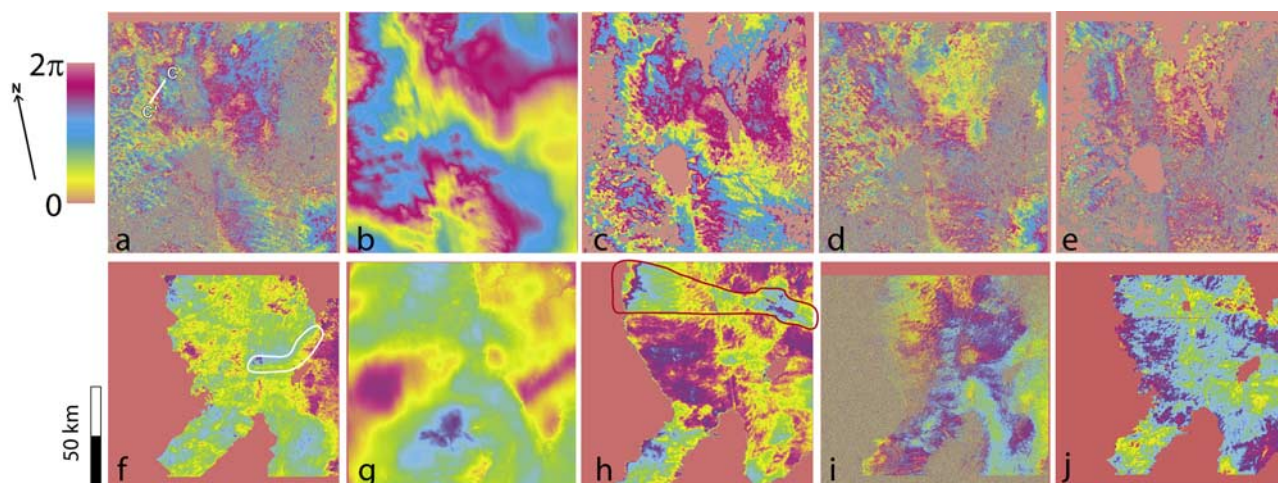
Figure 6. (a) Wrapped interferogram on Tiberias Lake region (frame 2943, see location on Figure 1) between 4 January 2004 and 14 March 2004. CC′ denotes profile of Figure 7. There are more than two fringes on this interferogram. (b) Same interferogram simulated from MM5. Some long-wavelength patterns are well reproduced. (c) MERIS simulation of the wrapped interferogram. The waves on the northwest of the lake are accurately reproduced. Pink mask is over water areas or cloudy pixels. Cloud signal is clearly visible on the interferogram. (d) Wrapped interferogram compensated by MM5 correction. There is one fringe less in the north-south direction after correction. (e) Wrapped interferogram compensated by MERIS simulation. Oscillations are wiped out and the residual signal is within a fringe. Low frequencies are correctly modeled (Figures 6d and 6e). (f-j) Same as Figures 6a to 6e for the couple 19 January 2003 and 30 March 2003 on frame 2907 (see location on Figure 1). A meteorological feature circled in white (Figure 6f) is well reproduced by the combined approach (Figure 6h) and not by MM5 alone (Figure 6g). However, in the area circled in red in Figure 6h, MERIS underestimated delay associated with 19 January 2003 due to undetected clouds.

[30] The greatest differences occur on cloudy pixels not detected by MERIS algorithm (see section 3.2 and the discrepancies on Figure 3 near Tiberias Lake on 26 October 2003). Some differences also result from mismodeling by MM5 which generally cannot be identified. In one particular case (see Figure 4b), we can infer that MM5 underestimated water vapor content due to uncertainties on land parameters (soil moisture) over the intensively cultivated Hula Basin. Typical high level of crops irrigation at this date (1 August 2004) may have yielded a significant increase of atmospheric water content. Here, MM5 estimate of W is 0.4 g cm^{-2} below that estimated from MERIS. Such local anthropogenic phenomena (about 25 km width) are not included in MM5 meteorological input data whose resolution is about 100 km. As noted by *Zhong et al.* [2005], MM5 humidity errors are partly due to lack of knowledge of the soil moisture. Thus we cannot expect MM5 to correctly model humidity in irrigated regions.

[31] Maps of the two estimates of W have been correlated and the results are presented in Table 3. As the three parameterizations show similar results, we chose to run MM5 with the first one for all dates. The correlation ranges from 0.42 to 0.94 with the best scores during summer. The mean difference is 0.036 g cm^{-2} and the standard deviation 0.21 g cm^{-2}. In order to assess the impact of cloud misdetection by MERIS, the correlation was calculated again by manually discarding automatically undetected cloudy pixels. As a result, the score dramatically improves for days when many clouds were not detected and is always greater than 0.79. The mean difference becomes $-5.2 \times$

10^{-3} g cm^{-2} and the standard deviation 0.19 g cm^{-2}, which is on the same order as the theoretical accuracy of MERIS algorithm (0.17 g cm^{-2}) [*Bennartz and Fischer*, 2001].

[32] On clear-sky zones, the bias between the two estimates is thus negligible: The two estimates are compatible and complementary because MM5 provides an estimate of W for cloudy pixels, contrarily to MERIS which in turn has a better resolution than MM5.

[33] Estimate of W should benefit from enhanced radiometric measurements and meteorological models, including the newly released Weather Research and Forecasting Model (WRF) [*Skamarock et al.*, 2005]. In similar contexts,
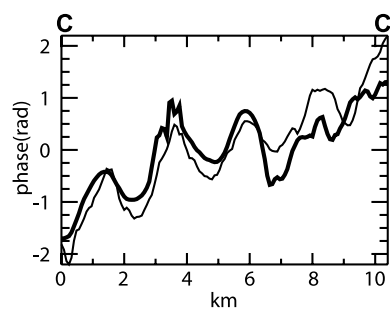

Figure 7. Profiles CC′ (see Figure 6 for location) of the interferogram (thin line) and of the interferogram simulated by MERIS and MM5 (thick line). The profiles have been averaged on a 10 km long segment perpendicular to CC′. Oscillations 2.25 km in wavelength superimpose well and have approximately the same amplitude (about 1 rad).
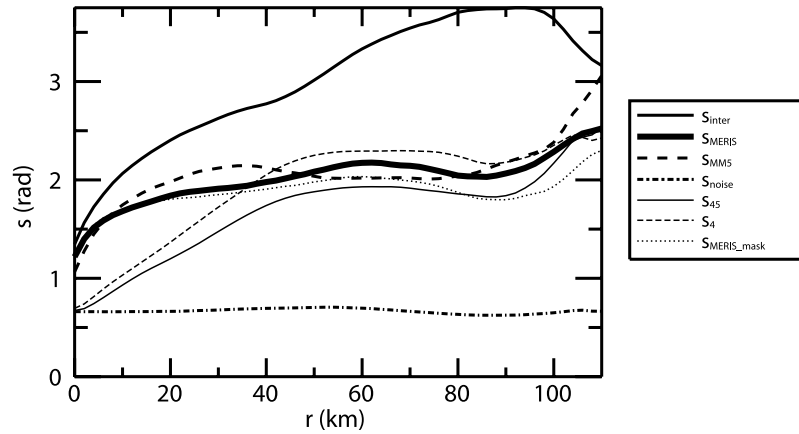
Figure 8. Energy $s(r)$ of the interferometric phase as a function of spatial wavelength r, averaged over four interferograms (see section 6 for details). The s_{inter} is the energy of the original interferograms; s_{MM5} is after correction by MM5; s_{MERIS} is after correction by MM5 and MERIS; s_{MERIS_mask} is after correction by MM5 and MERIS computed on a mask discarding undetected cloudy pixels; s_{noise} is computed from a flat interferogram with additive noise related to the coherence of the interferograms; s_{45} and s_4 are computed for 45 and 4 synthetic stacked interferograms, respectively. Stack of a minimum of four interferograms required to reach the average performance of the proposed atmospheric correction; $s(r)$ is reduced over most spatial wavelengths. Mean atmospheric correction is 0.93 rad for MM5 (respectively 1.0 rad for MM5 combined to MERIS).

advanced analysis of hyperspectral images yields measurements of W with an accuracy as low as 0.07 g cm^{-2} [*Marion et al.*, 2006]. One interferometric fringe approximately corresponds to 0.5 g cm^{-2} in C band. An enhanced spectrometer with a 0.01 g cm^{-2} accuracy operating simultaneously with a SAR instrument would be useful for filtering out atmospheric signal in clear-sky conditions.

5. Comparison With Other Techniques

5.1. Nonhydrostatic Versus Hydrostatic Estimate of the Phase Delay

[34] Other authors have developed methods based on static models of the atmosphere [*Baby et al.*, 1988; *Delacourt et al.*, 1998; *Remy et al.*, 2003]. For example, *Remy et al.* [2003] estimated the tropospheric delay by correlation with topography. In those models, the relative humidity is supposed to be homogeneous through the atmosphere and estimates of the phase delay vary only as a function of elevation (they are the same at all pixels with the same ground elevation). Thus variation of tropospheric delays induced by the dynamics of the atmosphere cannot easily be taken into account by those methods while numerous dynamical signal have been reported on SAR interferograms [*Hanssen et al.*, 1999].

[35] We compare here the phase delay estimation method presented in section 3 with the one developed by *Delacourt et al.* [1998]. The latter one is based on models by *Baby et al.* [1988] and uses ground meteorological measurements at a reference location. Pressure, relative humidity and temperature at this location are noted P_{g0} (mbar), U_{g0}, and T_{g0} (K), respectively. Δh is the elevation difference between a point and the reference. *Delacourt et al.* [1998] then estimate the hydrostatic delay ΔL_h (m) as

$$\Delta L_h = \frac{2.27 \times 10^{-3}}{\cos\theta} P_{g0}\left(1 - 22.6 \times 10^{-6}\Delta h\right)^{5.26}, \quad (9)$$

and the wet delay ΔL_w as

$$\Delta L_w = \frac{\nu}{\cos\theta} U_{g0} 10^{\gamma\left(T_{g0}-273-k\Delta h\right)}, \quad (10)$$

where k is the gradient of T with elevation, and γ and ν are latitude- and climate-dependent constants [*Baby et al.*, 1988].

[36] Figure 5 shows the mean radar delay calculated from MM5 on frame 2907 for 10 dates, the best fitting delay computed from *Delacourt et al.* [1998], and the residual. The residual shows systematically more humidity between the sea and the mountain ranges than behind them. This is a stationary meteorological effect which cannot be modeled by the static model of *Delacourt et al.* [1998]. Consequently, this stationary meteorological residue remains when a simple elevation-dependent delay is subtracted or even with interferogram stacking if the acquisition dates do not sample the year regularly. The mean difference (133 rad) comes from the fact that we model the tropospheric delay until 15 km only, whereas *Baby et al.* [1988] integrate the delay until pressure vanishes. High-frequency patterns on the residual are due to different processing of DEM for producing Figures 5a and 5b.

5.2. Comparison With Interferogram Stacking

[37] To evaluate the efficiency of interferogram stacking, we simulated 10 phase delays on frame 2907 as explained in section 3.1. We assumed that all the interferograms combining the 10 dates were feasible and computed 45 synthetic atmospheric interferograms. Their standard deviation is on average 4.42 rad. Results are presented in section 6.

6. Correction of Interferograms

[38] Six ENVISAT ASAR interferograms have been compensated by the proposed method. They have been unwrap-

ped after masking noisy parts where coherence level is too low. Uncertainty of few centimeters on orbits may yield a second-order polynomial artefact on the interferograms and requires baseline tuning [*Scharroo*, 2002]. Baseline tuning has been performed so that the best fit second-order polynomial of the interferograms equals that of the interferograms modeled from MM5.

[39] Figure 6 shows two typical results of the correction methods. The low frequencies of the interferogram are correctly modeled using MM5 alone or MM5 and MERIS combination (see Figures 6d, 6e, 6i and 6j). Some local atmospheric artefacts are correctly filtered out (see Figures 6 and 7). For example, an oscillation with amplitude as low as 1 rad and with 2.25 km wavelength, probably resulting from convective rolls, has been correctly modeled by MM5 coupled to MERIS. On the profile shown on Figure 7, the residual difference between the model and the interferogram has a standard deviation of 0.44 rad, which is less than the 2.46 rad wet delay standard deviation expected from MERIS theoretical accuracy (0.17 g cm^{-2}) (see section 2.2). Actually, the relative accuracy of W_{MERIS} must be better than the theoretical one because it may include systematic errors. For example, *Ciotti et al.* [2003] found that MERIS systematically underestimated W in comparison to ground-based measurements. Moreover, W_{MERIS} theoretical accuracy estimated by *Bennartz and Fischer* [2001] includes the effect of varying surface reflectance leading to systematic errors for a given surface: This type of error has less impact in our case as we subtract two delay maps deriving from W_{MERIS}.

[40] We then analyze the performance of the atmospheric filter with spatial wavelength. Because our atmospheric filter does not reduce the high-amplitude temporal decorrelation noise and because masked areas prevent the use of standard Fourier analysis techniques, we used a dedicated estimator $s(r)$ for an unwrapped interferogram f:

$$s(r) = \frac{\sum\limits_{i,j/d(i,j)=r} |f(i) - f(j)|}{N_r}, \qquad (11)$$

where r is a positive number denoting the spatial wavelength, i and j are unmasked pixels of the image, $d(i, j)$ is the Euclidian distance between i and j and N_r is the number of pairs such that $d(i, j) = r$. This criterion measures the mean absolute value of the difference between two pixels distant of r and can be seen as an energy function. When applied to a corrected interferogram the smaller $s(r)$ the better the atmospheric correction at spatial wavelength r. In order to evaluate the performance of the correction, we considered four out of the six processed interferograms and their corrections.

[41] For each interferogram, we computed s for the original interferogram and for the corrected ones on a common mask. Then s was averaged on the four selected interferograms: The averaged s on the original interferograms, on the versions corrected by MM5 alone and on those corrected by MERIS and MM5, are noted s_{inter}, s_{MM5}, and s_{MERIS}, respectively. Results are reported in Figure 8.

[42] The means of s_{inter}, s_{MM5}, and s_{MERIS} are 3.00, 2.07, and 2.0 rad, respectively. We assume here that there is no significant deformation signal on the four selected interfero-

grams in comparison with the meteorological signal. The correction has thus decreased s by 30%. The correction is effective for almost every frequency and the reduction attains a maximum of 1.67 rad for MM5 at r = 82 km (respectively 1.71 rad for MERIS and MM5 combination at r = 86 km). Note that both methods have similar performances (though slightly better in the second case) even for r between 300 m (MERIS resolution) and 2 km (MM5 simulation resolution). We expected a better correction from the combined approach for these wavelengths but the noise on W_{MERIS} does not allow a better performance. It is due in particular to misdetection of cloudy pixels by MERIS (see Figure 6h). To check this, we computed s_{MERIS} again in areas with no undetected cloudy pixels and noted it s_{MERIS_mask}. It is then always smaller than s_{MM5} (see Figure 8) and its mean is 1.88 rad.

[43] In order to evaluate the energy $s(r)$ of decorrelation noise, we simulated for each of the four analyzed interferograms a flat interferogram i_{noise} with additive Gaussian noise of standard deviation $\sigma_{\Delta\phi}$ computed from [*Rodriguez and Martin*, 1992]

$$\sigma_{\Delta\phi} = \frac{1}{\sqrt{2N}} \frac{\sqrt{1 - \rho^2}}{\rho}, \qquad (12)$$

where ρ is the coherence of the interferogram and N is the number of looks. After averaging, s was computed and noted s_{noise}. It is almost constant with wavelength and has a mean of 0.67 rad; s_{noise} represents the lower limit that a filter can attain. The best filter would decrease s by 2.33 rad in average. Thus the proposed approach reduces s by 43% of the maximal achievable reduction. If we consider the correction after masking of undetected cloudy pixels, 48% of the atmospheric signal has been removed. The remaining signal can result from external sources such as small ground deformation, ionospheric effects, unwrapping errors. It also comes from modeling errors, including aerosol effects on MERIS evaluation of W, uncertainty on meteorological parameters modeled by MM5, registration errors between MERIS images and interferograms.

[44] Results are compared to stacks of interferograms (see section 5.2). Stack of four independent interferograms yields noise reduction equivalent to the proposed atmospheric correction applied to a single interferogram (Figure 8). Stack of 45 nonindependent interferograms leads to a better correction than our filter applied to one interferogram especially for r less than 50 km. However, the correction is almost equivalent for r greater than 50 km, although stacking would give better results if the interferograms were all independent.

7. Discussion and Conclusion

[45] We developed an atmospheric filter dedicated to SAR interferometry which is based on the estimate of tropospheric delay from meteorological modeling and multispectral images acquired simultaneously with the SAR images. The maps of integrated water vapor content derived from MERIS or MM5 are shown to be consistent to 0.2 g cm^{-2} (RMS) and complementary. The proposed approach allows filtering of small amplitude atmospheric oscillations 2.25 km in wavelength and allows significant

noise reduction at all spatial wavelengths by about 1.0 rad on average. The filter is shown to be more effective than previously proposed techniques based on the assumption of a static atmosphere. Our approach is limited by data availability, cloud coverage, sensor detection level and resolution of meteorological models. Our study shows additionally that, as pointed out by other authors [*Hanssen et al.*, 1999], SAR interferometry can be used to analyze small-scale meteorological effects. Our approach that estimates the atmospheric phase delay should significantly improve the potential of SAR interferometry for the measurements of tectonic deformation, in particular interseismic deformation, where strong atmospheric effects are currently a major source of limitation.

References

American Meteorological Society (AMS) (2000), *Glossary of Meteorology*, Boston, Mass.

Askne, J., and H. Nordius (1987), Estimation of tropospheric delay for microwaves from surface weather data, *Radio Sci.*, *22*, 379–386.

Baby, H. B., P. Golé, and J. Lavergnat (1988), A model for the tropospheric excess path length of radio waves from surface meteorological measurements, *Radio Sci.*, *23*, 1023–1038.

Bennartz, R., and J. Fischer (2001), Retrieval of columnar water vapour over land from backscattered solar radiation using the Medium Resolution Imaging Spectrometer, *Remote Sens. Environ.*, *78*, 274–283.

Bonforte, A., A. Ferretti, C. Prati, G. Puglisi, and F. Rocca (2001), Calibration of atmospheric effects on SAR interferograms by GPS and local atmosphere models: First results, *J. Atmos. Sol. Terr. Phys.*, *63*, 1343–1357.

Ciotti, P., et al. (2003), Validation of MERIS water vapour in the central Italy by concurrent measurements of microwave radiometers and GPS receivers, paper presented at IGARSS, Inst. of Electr. and Electron. Eng., Toulouse, France.

Daëron, M., L. Benedetti, P. Tapponnier, A. Sursock, and R. C. Finkel (2004), Constraints on the post ~25-ka slip rate of the Yammoûneh fault (Lebanon) using in situ cosmogenic ^{36}Cl dating of offset limestone-clast fans, *Earth Planet. Sci. Lett.*, *227*, 105–119.

Delacourt, C., P. Briole, and J. Achache (1998), Tropospheric corrections of SAR interferograms with strong topography. Application to Etna, *Geophys. Res. Lett.*, *25*, 2849–2852.

Ducic, V. (2004), Tomographie de l'ionosphère et de la troposphère à partir des données GPS denses: Applications aux risques naturels et amélioration de l'interférométrie SAR, Ph.D. thesis, 331 pp., Univ. Paris 7–Denis Diderot, Paris.

Dudhia, J. (1996), A multi-layer soil temperature model for MM5, paper presented at the Sixth PSU/NCAR Mesoscale Model Users' Workshop, Natl. Center for Atmos. Res., Boulder, Colo., 22–24 July.

Emardson, T. R., and H. J. P. Derks (2000), On the relation between the wet delay and the integrated precipitable water vapour in the European atmosphere, *Meteorol. Appl.*, *7*, 61–68.

Emardson, T. R., M. Simons, and F. H. Webb (2003), Neutral atmospheric delay in interferometric synthetic aperture radar applications: Statistical description and mitigation, *J. Geophys. Res.*, *108*(B5), 2231, doi:10.1029/2002JB001781.

European Space Agency (ESA) (2004), MERIS Product Handbook, Paris.

Fischer, J., and R. Bennartz (1997), Retrieval of total water vapour content from MERIS measurements, ATBD 2.4, Eur. Space Agency, Paris.

Fritsch, J. M., and C. F. Chappell (1980), Numerical prediction of convectively driven mesoscale pressure systems. part I: Convective parameterization, *J. Atmos. Sci.*, *37*, 1722–1733.

Grell, G. A., et al. (1995), A description of the fifth-generation Penn State/NCAR Mesoscale Model (MM5), *NCAR Tech. Note, NCAR/TN-398 + STR*.

Hanssen, R. (2001), *Radar Interferometry: Data Interpretation and Error Analysis*, Springer, New York.

Hanssen, R. F., T. M. Weckwerth, H. A. Zebker, and R. Klees (1999), High-resolution water vapor mapping from interferometric radar measurements, *Science*, *283*, 1297–1299.

Hanssen, R., I. Weinreich, S. Lehner, and A. Stoffelen (2000), Tropospheric wind and humidity derived from spaceborne radar intensity and phase observations, *Geophys. Res. Lett.*, *27*, 1699–1702.

Hong, S.-Y., and H.-L. Pan (1996), Nonlocal boundary layer vertical diffusion in a medium-range forecast model, *Mon. Weather Rev.*, *124*, 2322–2339.

Janjic, Z. I. (1990), The step-mountain coordinate: Physical package, *Mon. Weather Rev.*, *118*, 1429–1443.

Janjic, Z. I. (1994), The step-mountain Eta coordinate model: Further developments of the convection, viscous sublayer, and turbulence closure schemes, *Mon. Weather Rev.*, *122*, 927–945.

Kain, J. S., and J. M. Fritsch (1993), Convective parameterization for mesoscale models: The Kain-Fritsch scheme, in *The Representation of Cumulus Convection in Numerical Models*, p. 246, Am. Meteorol. Soc., Washington, D. C.

Kistler, R., et al. (1999), The NCEP/NCAR 50-year reanalysis, *Bull. Am. Meteorol. Soc.*, *82*, 247–268.

Klinger, Y., et al. (2000), Slip rate on the Dead Sea transform fault in northern Araba valley (Jordan), *Geophys. J. Int.*, *142*, 755–768.

Li, Z., J.-P. Muller, P. Cross, and E. J. Fielding (2005), Interferometric synthetic aperture radar (InSAR) atmospheric correction: GPS, Moderate Resolution Imaging Spectroradiometer (MODIS), and InSAR integration, *J. Geophys. Res.*, *110*, B03410, doi:10.1029/2004JB003446.

Li, Z., J-P. Muller, P. Cross, P. Albert, J. Fischer, and R. Bennartz (2006a), Assessment of the potential of MERIS near-infrared water vapour products to correct ASAR interferometric measurements, *Int. J. Remote Sens.*, *27*, 349–365.

Li, Z., E. J. Fielding, P. Cross, and J.-P. Muller (2006b), Interferometric synthetic aperture radar atmospheric correction: GPS topography-dependent turbulence model, *J. Geophys. Res.*, *111*, B02404, doi:10.1029/2005JB003711.

Li, Z., E. J. Fielding, P. Cross, and J.-P. Muller (2006c), Interferometric synthetic aperture radar atmospheric correction: Medium Resolution Imaging Spectrometer and Advanced Synthetic Aperture Radar integration, *Geophys. Res. Lett.*, *33*, L06816, doi:10.1029/2005GL025299.

Lohman, R. B., and M. Simons (2005), Some thoughts on the use of InSAR data to constrain models of surface deformation: Noise structure and data downsampling, *Geochem. Geophys. Geosyst.*, *6*, Q01007, doi:10.1029/2004GC000841.

Marion, R., R. Michel, and C. Faye (2006), Atmospheric correction of hyperspectral data over dark surfaces via simulated annealing, *IEEE Trans. Geosci. Remote Sens.*, *44*(6), 1566–1574.

Massonnet, D., and T. Rabaute (1993), Radar interferometry: Limits and potential, *IEEE Trans. Geosci. Remote Sens.*, *31*, 455–464.

Massonnet, D., M. Rossi, C. Carmona, F. Adragna, G. Peltzer, K. Feigl, and T. Rabaute (1993), The displacement field of the Landers earthquake mapped by radar interferometry, *Nature*, *364*, 138–142.

Moisseev, D., and R. Hanssen (2003), Towards an atmosphere-free interferogram; first comparison between ENVISAT's ASAR and MERIS water vapor observations, paper presented at International Geoscience and Remote Sensing Symposium, Inst. of Electr. and Electron. Eng., Toulouse, France, 21–25 July.

Pleim, J. E., and J. S. Chang (1992), A non-local closure model for vertical mixing in the convective boundary layer, *Atmos. Environ.*, *26*, 965–981.

Remy, D., S. Bonvalot, P. Briole, and M. Murakami (2003), Accurate measurements of tropospheric effects in volcanic areas from SAR interferometry data: Application to Sakurajima volcano (Japan), *Earth Planet. Sci. Lett.*, *6730*, 1–12.

Rignot, E., D. Braaten, S. P. Gogineni, W. B. Krabill, and J. R. McConnell (2004), Rapid ice discharge from southeast Greenland glaciers, *Geophys. Res. Lett.*, *31*, L10401, doi:10.1029/2004GL019474.

Rodriguez, E., and J. M. Martin (1992), Theory and design of interferometric synthetic aperture radars, *IEE Proc., Part F, Radar Signal Processing*, *139*, 147–159.

Rögnvaldsson, Ó. (2005), MM5IDL: A flexible framework for post-processing MM5 data, paper presented at 21st Conference on Weather Analysis and Forecasting/17th Conference on Numerical Weather Prediction, Am. Meteorol. Soc., Washington, D. C., 31 July to 5 Aug.

Scharroo, R. (2002), *Decade of ERS Satellite Orbits and Altimetry*, 213 pp., Delft Univ. Press, Delft, Netherlands.

Skamarock, W. C., J. B. Klemp, J. Dudhia, D. O. Gill, D. M. Barker, W. Wang, and J. G. Powers (2005), A description of the advanced research WRF version 2, *NCAR Tech. Note, NCAR/TN–468+STR*, 100 pp.

Skone, S., and M. E. Cannon (1999), Ionospheric effects on differential GPS applications during auroral substorm activity, *ISPRS J. Photogramm. Remote Sens.*, *54*, 279–288.

Smith, E. K., and S. Weintraub (1953), The constants in the equation for atmospheric refractive index at radio frequencies, *J. Res. Natl. Bur. Stand.*, *50*, 39–41.

Solheim, F. S., J. Vivekanandan, R. H. Ware, and C. Rocken (1999), Propagation delays induced in GPS signals by dry air, water vapor, hydrometeors, and other particulates, *J. Geophys. Res.*, *104*, 9663–9670.

Stauffer, D. R., et al. (1991), Use of four-dimensional assimilation in a limited-area mesoscale model. part II: Effects of data assimilation within the planetary boundary layer, *Mon. Weather Rev.*, *119*, 734–754.

Williams, S., Y. Bock, and P. Fang (1998), Integrated satellite interferometry: Tropospheric noise, GPS estimates and implications for interferometric synthetic aperture radar products, *J. Geophys. Res.*, *103*, 27,051–27,068.

Wright, T., B. Parsons, and E. Fielding (2001), Measurement of interseismic strain accumulation across the North Anatolian Fault by satellite radar interferometry, *Geophys. Res. Lett.*, *28*, 2117–2120.

Wright, T. J., B. Parsons, P. C. England, and E. J. Fielding (2004), InSAR observations of low slip rates on the major faults of western Tibet, *Science*, *305*, 236–239.

Xiu, A., and J. E. Pleim (2001), Development of a land surface model. part I: Application in a mesoscale meteorological model, *J. Appl. Meteorol.*, *40*, 192–209.

Zhong, S., et al. (2005), Evaluation of real-time high-resolution MM5 predictions over the Great Lakes region, *Weather Forecast.*, *20*, 63–81.

———————————

J.-P. Avouac, Tectonics Observatory, Geological and Planetary Sciences Division, California Institute of Technology, Mail Code 100-23, Pasadena, CA 91125, USA.

R. Michel and B. Puysségur, Laboratoire de Détection et de Géophysique, CEA, BP 12, F-91680 Bruyères-le-Châtel Cedex, France. (beatrice.puyssegur@cea.fr)